Check for updates

ADVANCED MATERIALS
www.advmat.de

Dynamic Behavior of Spatially Confined Sn Clusters and Its Application in Highly Efficient Sodium Storage with High Initial Coulombic Efficiency

Haoqing Ma, Ruohan Yu, Wangwang Xu, Lei Zhang, Jinghui Chen, Bomian Zhang, Jiantao Li, Xu Xu, Qinyou An,* Weina Xu, Lu Ma, Kumar Varoon Agrawal, and Kangning Zhao**

Advanced battery electrodes require a cautious design of microscale particles with built-in nanoscale features to exploit the advantages of both micro- and nano-particles relative to their performance attributes. Herein, the dynamic behavior of nanosized Sn clusters and their host pores in carbon nanofiber) during sodiation and desodiation is revealed using a state-of-the-art 3D electron microscopic reconstruction technique. For the first time, the anomalous expansion of Sn clusters after desodiation is observed owing to the aggregation of clusters/single atoms. Pore connectivity is retained despite the anomalous expansion, suggesting inhibition of solid electrolyte interface formation in the sub-2-nm pores. Taking advantage of the built-in nanoconfinement feature, the CNF film with nanometer-sized interconnected pores hosting Sn clusters (≈2 nm) enables high utilization (95% at a high rate of 1 A g^{-1}) of Sn active sites while maintaining an improved initial Coulombic efficiency of 87%. The findings provide insights into electrochemical reactions in a confined space and a guiding principle in electrode design for battery applications.

1. Introduction

Recently, Na-ion batteries have received considerable attention owing to their potential benefits of revolutionarily low-cost, safe, and scalable energy-storage technologies.[1] The use of Na as an inexpensive and abundant element for charge carriers compared to Li makes it attractive for applications unconcerned with weight/volume. Owing to their great similarity with Li-ion batteries in terms of working principles,[2] the commercialization of Na-ion batteries is anticipated to be swift, relying on the current technologies available for Li-ion batteries. However, most commercialized Li-ion batteries use graphite as the anode, which cannot host the larger and more polarized Na^+ cations. Therefore, an alternative anode material is required for replacement or modification.[3] As an alternative, Sn-based alloying reaction with Na ions has received considerable interest due to its high theoretical capacity (847 mAh g^{-1}), large bulk density (7.28 g cm^{-3}), and low operation voltage (0.3–0.4 V).[4] However, the high intake/output of Na ions (3.75 Na^+ per Sn) into the host can result in a large volume expansion and contraction (≈420%), which can cause mechanical failure of Sn particles. Additionally, electrolyte decomposition and an inevitable solid electrolyte interface (SEI) layer formation on the Sn electrode and electrolyte interface can occur because the working voltage of Sn falls below 1 V.[5] The breakdown of larger Sn particles can result in fresh surface exposure to the electrolyte,

H. Ma, R. Yu, L. Zhang, J. Chen, B. Zhang, J. Li, X. Xu, Q. An
State Key Laboratory of Advanced Technology for Materials Synthesis and Processing
Wuhan University of Technology
Wuhan 430070, P. R. China
E-mail: zhanglei1990@whut.edu.cn; anqinyou86@whut.edu.cn

H. Ma, L. Zhang, J. Chen, B. Zhang
The Sanya Science and Education Innovation Park of Wuhan University of Technology
Sanya 572000, P. R. China

W. Xu
Department of Mechanical Engineering
Louisiana State University
Baton Rouge, LA 70803, USA

The ORCID identification number(s) for the author(s) of this article can be found under https://doi.org/10.1002/adma.202307151

DOI: 10.1002/adma.202307151

W. Xu
School of Material Science and Engineering
Dongguan University of Technology
Dongguan 523808, China

L. Ma
National Synchrotron Light Source II
Brookhaven National Laboratory
Upton, NY 11973, USA

K. V. Agrawal, K. Zhao
Laboratory of Advanced Separations
École polytechnique fédérale de Lausanne
Sion 1950, Switzerland
E-mail: kangning.zhao@epfl.ch

 © 2024 Wiley-VCH GmbH

causing a more insulating SEI layer formation.[6] More SEI layer is detrimental to electrolyte consumption and causes loss of the active Sn electrode due to electrical isolation. Consequently, such batteries display a low initial Coulombic efficiency (CE),[7] fast capacity decay, and limited cycle life. Therefore, a rational design of Sn electrode for Na-ion batteries is required to achieve a high energy density.

Electrode design is controversial, and the benefits of nanostructured electrodes for practical battery applications have been researched. By downsizing electrodes into nanosized particles, clusters, or single atoms, electrode kinetics can be greatly facilitated. Thus, the utilization of Sn active sites should be high to enable high capacity, particularly at high currents. Additionally, the mechanical stability of nanosized particles with resistance to stress-induced cracking and pulverization should be improved.[8] However, a nanosized electrode with a higher contact area to its electrolyte promotes side reactions between each other.[9] Thus, CE, particularly for the first cycle, is fairly low (usually below 80%) and severely reduces the full battery cycle life in practical applications. Previous studies suggest that micron-sized electrodes expose less surface area to the electrolyte to obtain high CE,[4] while electrode capacity (utilization) is traded off. The use of microscale particles with nanoscale attributes has been proposed to combine the merits of nanoscale attributes.[10] For instance, Shi et al.[11] incorporated intrinsic nanopores into a metal-organic framework to host Sn atoms and achieved high utilization of active sites and reaction kinetics while avoiding the agglomeration of Sn. However, the framework was unstable during the reaction, which led to a lower CE. The same limitation remains to be a challenge on microscale structure design with nanoscale features[12] to combine their merits.

Herein, we report the synthesis of carbon nanofiber (CNF) films with interconnected open pores to host Sn clusters of sizes mostly below 2 nm and enable a high initial CE of 87%, while maintaining high utilization of Sn active sites for over 95% at a high current of 1 A g^{-1}. By utilizing the advantages of deep learning-assisted sub-nanometer spatial resolution 3D high-angle annular dark-field scanning transmission electron microscopy (3D HAADF-STEM) reconstruction technique, we unambiguously reveal CNF films with gradient, interconnected, and open-pore confined Sn clusters (below 2 nm). The pores inside the CNF films are flexible and remain interconnected, whereas the Sn particles remain isolated, as revealed by the 3D reconstruction of a sample after sodiation and desodiation. Notably, the dead pore percentage is negligible, ensuring Na-ion transport in the CNF films, particularly in the central area. Thus, high utilization (95%) of Sn active sites is achieved at a high rate. Moreover, the small size (below 2 nm) of the pores limits electrolyte decomposition, thereby affecting SEI layer formation inside the CNF film, which improves the initial CE to 87%.

2. Results and Discussion

Sn–CNF were prepared using the electrospinning method. An as-spun film was self-supported and could be easily scaled up, as illustrated in **Figure 1a**. The large-area Sn–CNF film could be bent back and forth several times without breaking (Figure S1, Supporting Information). The film was easy to handle and could be directly cut or rolled into electrodes without further processing, which significantly reduced the complexity of electrode fabrication. The scanning electron microscopy (SEM) image in Figure 1b showed continuous cross-linked nanofibers, providing good flexibility to the film. Each fiber had a diameter of ≈80 nm, and no obvious large particles were observed in the selected range. The energy dispersive spectrometer (EDS) mapping and spectra presented in Figure 1c and Figure S2, Supporting Information revealed Sn mapping within the range of CNFs, suggesting the successful incorporation of Sn inside the CNF pores. The high-resolution HAADF-STEM image illustrated in Figure 1c showed a large number of nanoparticles inside the CNF, where the bright dots suggested the presence of Sn atoms with high Z contrast inside the CNF pores. The magnified image shown in Figure 1d revealed Sn clusters of size ≈2 nm on the CNF surface. Furthermore, the electron energy loss spectroscopy (EELS) mapping (Figure S3, Supporting Information) revealed the uniform distribution of Sn in the CNF range, while the EELS spectrum (inset image in Figure 1d) suggested the metallic state of Sn with no detected O peaks.[13] The obtained results were in line with the X-ray diffraction (XRD) patterns (Figure S4, Supporting Information) of pure β-Sn. The Raman spectrum (Figure S5, Supporting Information) suggested that the CNFs were graphitized C with abundant defects. To obtain the mass percentage of Sn in the composite, thermogravimetric analysis in air revealed a high loading of Sn (53.9 wt%) in the Sn–CNFs (Figure S6 and Note S1, Supporting Information).

To further distinguish the existence of Sn clusters inside the CNF pores, 3D tomography reconstruction was performed, where 70 HAADF-STEM images were collected at 2° interval (Video S1, Supporting Information). The 3D image shown in Figure 1e revealed larger and smaller particles on the surface and central regions, respectively. Interactive thresholding was applied to determine pore, C, and Sn particles based on a grayscale histogram (Figure S7, Supporting Information) and Z contrast from HAADF-STEM through the process flow shown in Figure S8, Supporting Information.[14] The gaps in the grayscale were easily distinguished as pore, C, and Sn particles. The ortho-slice of the *XZ*–axis showed distinguishable interconnected pores (white) in the CNF (blue) and Sn clusters (yellow) at the pore edges. Moreover, the particles were located at the edge rather than being fully encapsulated by C, leaving space for direct contact with the electrolyte. To quantify the cluster size, the Feret diameters method was applied. The length and width of Sn particles ranged from 0.25 to 4.00 nm, suggesting the existence of Sn as mostly clusters (Figure S9, Supporting Information). Moreover, the number of Sn particles was evidently greater at the edge than at the center. Thus, to further quantify the pores and Sn clusters inside and outside the CNF, slices of subvolumes 1 and 2 at the center and edge of the CNF were obtained, respectively, by volume fraction and Feret diameters method, as shown in Figure 1f. The slices were extracted from the main 3D tomography reconstruction image to identify the difference in pores. The pore volume decreased from 47.6 ± 1% in subvolume 2 to 32.1 ± 1% in subvolume 1, suggesting a decrease in pore diameter from the edge toward the central area. The pattern was similar to conical pores, which was considered beneficial for retaining electrolytes inside the pores. As the pores inside were relatively small, we determined the dead pores inside the CNF using the ambient occlusion computation method. The dead pore percentage in the CNF was less than

© 2024 Wiley-VCH GmbH

15214095, 0, Downloaded from https://onlinelibrary.wiley.com/doi/10.1002/adma.202307151 by li bai - Columbia University Libraries , Wiley Online Library on [27/02/2024]. See the Terms and Conditions (https://onlinelibrary.wiley.com/terms-and-conditions) on Wiley Online Library for rules of use; OA articles are governed by the applicable Creative Commons License

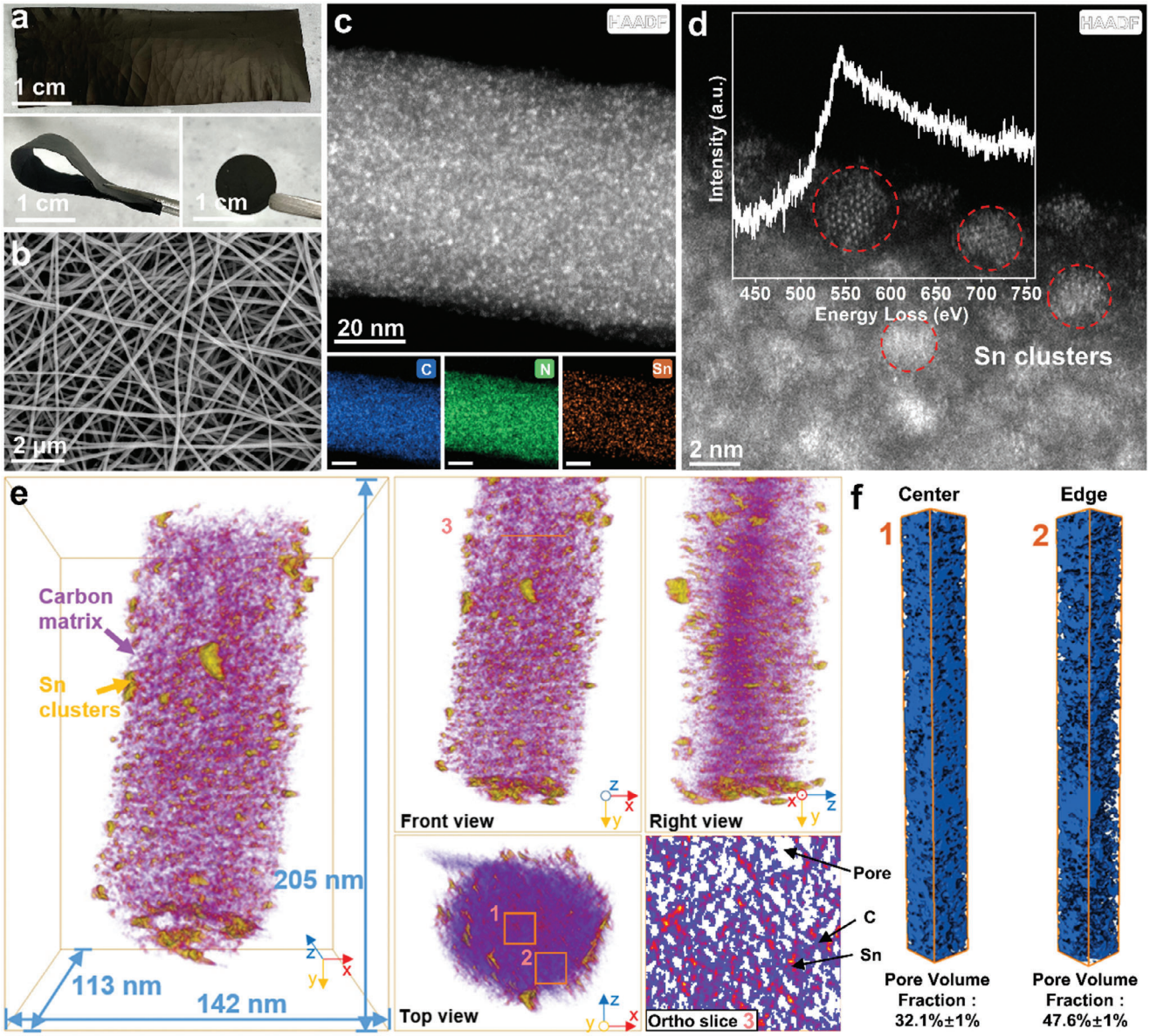

Figure 1. a) Optical images of Sn–CNF electrode. b) SEM image of Sn–CNF. c) HAADF image of Sn–CNF and EDS mapping. d) High-resolution HAADF image of Sn clusters and the inset image show the EELS spectrum of Sn. e) 3D tomography of Sn–CNF and 38.4 × 38.4 nm ortho slice of *XZ*–axis from position 3 in (e), front view. f) Subvolume from (e), top view positions 1 and 2, and pore volume fraction of the Sn–CNF at the center and edge, respectively.

1%, which was negligible (Figure S10, Supporting Information). Thus, the pores were interconnected and beneficial for electrolyte penetration into the CNF. Furthermore, the pore structure was confirmed through the Brunauer–Emmett–Teller (BET) test. The N_2 adsorption–desorption isotherm (Figure S11, Supporting Information) revealed an H4 shape curve and Sn–CNF with a surface area of 151.3 $m^2\ g^{-1}$ comprised micropores.[15]

The as-spun film was cut directly into electrodes for a Na-ion battery half-cell. The cell was first cycled at 100 mA $g_{Sn\text{-}CNF}{}^{-1}$, as shown in Figure 2a. A distinguished discharge plateau below 0.4 V was observed during sodiation, while during desodiation, four obvious potential plateaus at 0.18, 0.27, 0.53, and 0.69 V were observed, corresponding to the stepwise dealloying of $Na_{15}Sn_4$.[16] The observed results were consistent with those of cyclic voltammetry (CV) curves (Figure S12, Supporting Information), where the second and third scans almost overlapped, indicating good stability of Sn–CNF during electrochemical sodiation and desodiation. The first cycle showed discharge and charge capacities of 570.6 and 501.6 mAh $g_{Sn\text{-}CNF}{}^{-1}$, respectively, corresponding to a high initial CE (ICE) of 87.9%. ICE was consistent across 12 cells, with an average CE of 87% (Figure 2b). As shown in Figure 2c, the cycling stability at 1000 mA $g_{Sn\text{-}CNF}{}^{-1}$ revealed a stable capacity retention of 94.1% for over 50 cycles with an average CE of 99.8%. Notably, the capacity based on Sn retained at 807.9 mAh $g_{Sn}{}^{-1}$, corresponding to an ultra-high Sn utilization of 95% (Figure S13, Supporting Information and detailed

© 2024 Wiley-VCH GmbH

15214095, 0, Downloaded from https://onlinelibrary.wiley.com/doi/10.1002/adma.202307151 by li bai - Columbia University Libraries , Wiley Online Library on [27/02/2024]. See the Terms and Conditions (https://onlinelibrary.wiley.com/terms-and-conditions) on Wiley Online Library for rules of use; OA articles are governed by the applicable Creative Commons License

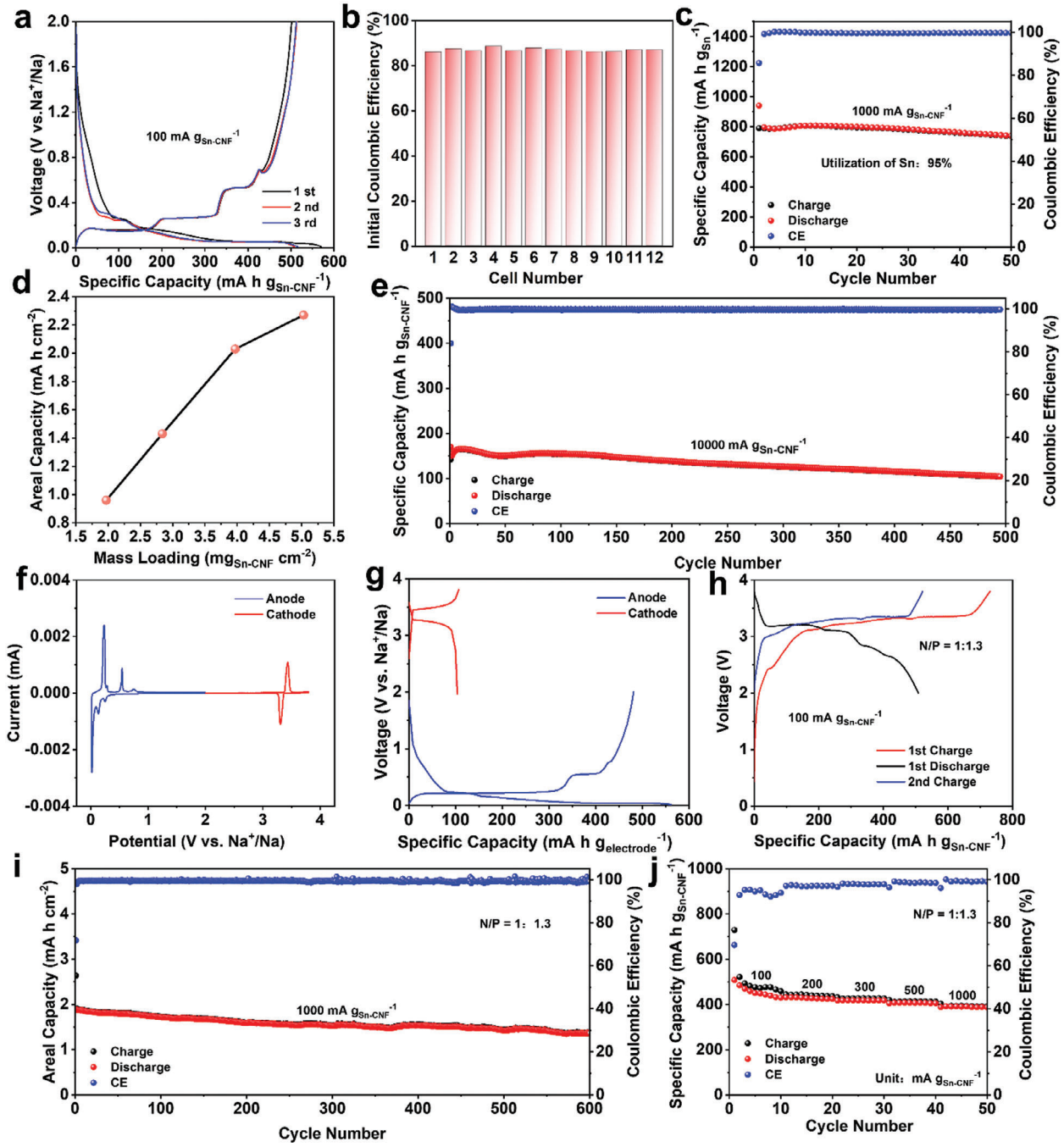

Figure 2. a) Galvanostatic discharge/charge profiles of the Sn–CNF electrode in the voltage range of 0.01–2 V versus Na^+/Na tested at a current density of 100 mA $g_{Sn\text{-}CNF}^{-1}$. b) ICE statistics of 12 cells. c) Cycling performance of Sn–CNF half-cell at 1000 mA $g_{Sn\text{-}CNF}^{-1}$. d) Areal capacity of Sn–CNF half-cell at different mass loading. e) Long-term cycle life at 10 000 mA $g_{Sn\text{-}CNF}^{-1}$ after initial 5-cycle activation at 1000 $g_{Sn\text{-}CNF}^{-1}$. f) CV curves scanned at a rate of 0.05 V s^{-1}. g) Galvanostatic discharge/charge profiles at 1000 mA g^{-1} of Sn–CNF and NVP half-cell. h) Galvanostatic discharge/charge profiles tested at 100 mA $g_{Sn\text{-}CNF}^{-1}$ of Sn–CNF electrode in the voltage range of 2–3.8 V versus NVP. i,j) Cycling performance and rate capability of Sn–CNF–NVP full-cell.

calculation process in Note S2, Supporting Information), outperforming the state-of-the-art Na-ion battery anode with high initial CE (Table S1, Supporting Information) and demonstrating potential applications in practical Na-ion battery. Notably, with an increase in mass loading, the capacity loss was minimal, and a high capacity could be maintained at a high mass loading of 5.03 $mg_{Sn\text{-}CNF}$ cm^{-2} to achieve a high areal capacity of 2.27 mAh cm^{-2}, as shown in Figure 2d. Furthermore, the long-term cycle life at a high current density of 10 A $g_{Sn\text{-}CNF}^{-1}$ after the initial 5-cycles of activation showed a capacity of 165 mAh $g_{Sn\text{-}CNF}^{-1}$ over 500 cycles, as shown in Figure 2e.

© 2024 Wiley-VCH GmbH

15214095, 0, Downloaded from https://onlinelibrary.wiley.com/doi/10.1002/adma.202307151 by li bai - Columbia University Libraries , Wiley Online Library on [27/02/2024]. See the Terms and Conditions (https://onlinelibrary.wiley.com/terms-and-conditions) on Wiley Online Library for rules of use; OA articles are governed by the applicable Creative Commons License

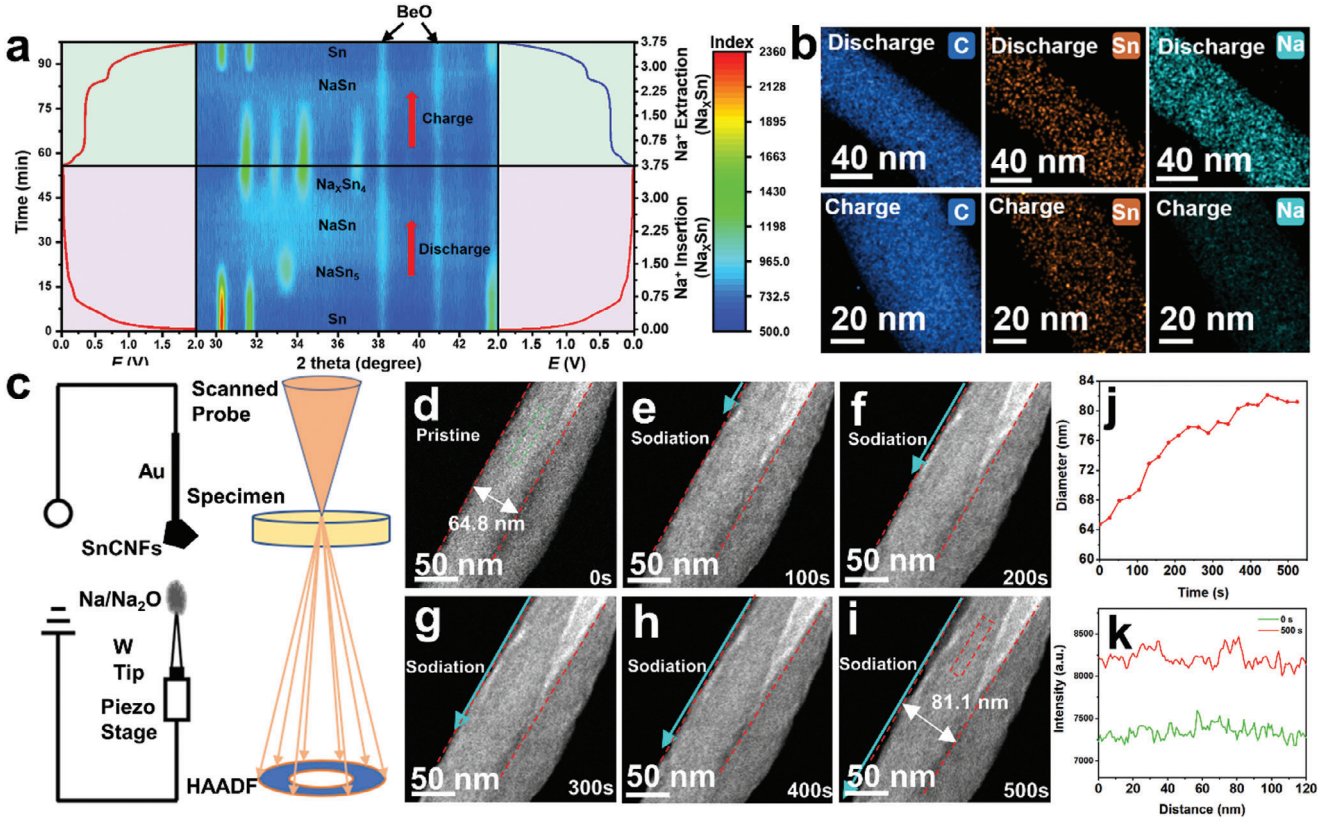

Figure 3. a) In situ XRD of Sn–CNF. b) TEM mapping of discharged and charged Sn–CNF. c) Schematic of in situ STEM characterization. d–i) Time-lapse in situ HAADF-STEM images of Sn–CNF during the first sodiation. j) Diameter change of Sn–CNF. k) Contrast intensity of marked area shown in (d) and (i).

Furthermore, to investigate the electrochemical performance, a full cell was assembled using Sn–CNF as the anode and $Na_3V_2(PO_4)_3$ (NVP) as the cathode. The voltage window of the full-cell was evaluated using CV, as shown in Figure 2f. Based on the potential of oxidation and reduction peaks, the voltage window of the full-cell was set at 2.00–3.80 V, under which the following tests for the full-cell were performed. Based on the galvanostatic discharge/charge profiles of the Sn–CNF and NVP half-cells, as shown in Figure 2g, N/P ratio was optimized to 1:1.3 (Figure S14, Supporting Information). The discharge/charge profiles of the full-cell at the N/P ratio of 1:1.3 and current density of 100 mA $g_{Sn\text{-}CNF}^{-1}$ are shown in Figure 2h. Four potential plateaus at 2.40, 3.11, 3.20, and 3.30 V in the first charge profile and those at 3.21, 3.12, 2.81, and 2.70 V in the discharge profile were consensus with the results of the half-cell, as shown in Figure 2a. To probe the full-cell stability, its long-term cycle life was tested at a current density of 1000 mA $g_{Sn\text{-}CNF}^{-1}$ and a practical areal capacity of 1.91 mAh cm^{-2}. The cell stably operated for over 600 cycles retaining an areal capacity of 1.37 mAh cm^{-2}, as shown in Figure 2i. The rate performance of the full-cell in Figure 2j revealed capacities of 450.3, 431.5, 418.1, 407.6, and 391.8 mAh $g_{Sn\text{-}CNF}^{-1}$ at current densities from 100 to 200, 300, 500 to 1000 mA $g_{Sn\text{-}CNF}^{-1}$. Furthermore, as a proof of concept, a 20 mAh pouch cell was assembled and it can light a digital image of a light-emitting diode lit with a working voltage of ≈3.10 V (Figure S15, Supporting Information). The rate capability and cycling performance of the NVP half-cell are shown in Figure S16, Supporting Information.

To probe the phase change in Sn–CNFs, in situ XRD in Figure 3a revealed three typical peaks at 30.3°, 31.7°, and 43.6°,[17] which corresponded to the (200), (101), and (220) planes of Sn metal, respectively. Within the initial 20 min, a two-phase reaction was observed, with the disappearance of the three major Sn peaks and the emergence of $NaSn_5$. After further sodiation for 10 min, $NaSn_5$ gradually disappeared and no other peak was observed except for the BeO peak from the Be window, suggesting the formation of an amorphous NaSn phase.[18] After full sodiation, the intensities of the peaks at 31.5°, 32.9°, 34.3°, and 37° increased, implying further sodiation of the Na_xSn_4 (x = 9–15) phase.[16] No other phases were detected. During desodiation, the Na_xSn_4 phase changed to amorphous NaSn after losing ≈2 Na^+. However, upon further desodiation, the amorphous NaSn was directly transformed to the Sn phase without the intermediate $NaSn_5$ owing to asymmetric kinetic effects.[18] To probe sodiation, TEM mapping (Figure 3b) of dis/charged Sn–CNF showed uniform dispersion of C, Sn, and Na during dis/charging, and the Na signal reduced after charging.

To probe the volume evolution of Sn–CNF during sodiation, in situ STEM characterization in Figure 3c was performed, where Sn–CNF was placed on an Au rod as the working electrode and Na/Na_2O was used as the counter and reference electrodes. A constant voltage was applied to drive the sodiation process, and

© 2024 Wiley-VCH GmbH

15214095, 0, Downloaded from https://onlinelibrary.wiley.com/doi/10.1002/adma.202307151 by li bai - Columbia University Libraries , Wiley Online Library on [27/02/2024]. See the Terms and Conditions (https://onlinelibrary.wiley.com/terms-and-conditions) on Wiley Online Library for rules of use; OA articles are governed by the applicable Creative Commons License

from the time-lapse HAADF-STEM images in Figure 3d–i, the diameter of Sn–CNF expanded from 64.8 to 81.1 nm in 500 s. The diameter change was severe in the initial 420 s and grew stable afterward (Figure 3j), suggesting the flexible buffering of CNF as a Sn host during sodiation. The intensity profiles collected from the green and red rectangles in the time-lapse images at 0 and 500 s are shown in Figure 3k. The increase in HAADF contrast intensity (10–15%) suggested the improvement in average atomic number contrast (Z-contrast), which proved Na insertion.[19]

Ex situ EELS was conducted to analyze the valence change of Sn (Figure S17, Supporting Information), where the ex situ EELS spectrum showed no obvious peak shift, confirming no valence change occurrence during discharging and charging. The evolution of Sn during sodiation and desodiation was also revealed through X-ray absorption near-edge structure (XANES) (Figure S18, Supporting Information). During sodiation, Sn was in the Sn^{-}-type oxidation state, which reverted to the pristine state during desodiation.[20] The extended X-ray absorption fine structure (EXAFS) suggested the introduction of a new peak at 1.5–2.2 Å by Na intercalation, which was related to Sn–N(Na, C).[20]

To further investigate the structural changes within the confinement, ex situ 3D tomography was performed, as shown in **Figure 4**. In Figure 4a–c, the pore volume in the sodiated state showed a slightly decreased pore volume of 25.8 ± 1%, which was predictable because sodiation brought more Na atoms into the CNF host. The cluster size increased with the insertion of Na + ions, as verified by the histogram of the cluster length and width (Figure S19, Supporting Information). The frequency of the cluster length below 2 nm decreased from 91.6 to 75.6%, confirming the increase in cluster size. Furthermore, the frequency of the pore length below 2 nm decreased from 97.2 to 80.2%, indicating an increase in pore size upon sodiation and revealing the flexible nature of CNF. The results were consistent with the in situ STEM characterization results presented in Figure 3d–i. Moreover, ortho-slice after sodiation revealed that the clusters remained at the pore edge without blocking the pores, while maintaining better contact with the electrolyte. After desodiation, the pore volume increased to 30.9 ± 1%, which was even higher than that of pristine sample. The pore length remained similar to that during the sodiated state, with no sign of recovering to the initial smaller pore length (Figure S20, Supporting Information). The combination of increased pore volume and pore length suggested the flexible nature of CNF in buffering the expansion and contraction of the clusters. The extra pore volume allowed for a better penetration of the electrolyte. The same was also confirmed by a reduced impedance (Figure S21 and Note S3, Supporting Information). Contrary to the traditional perspective that pores could get blocked by Na insertion, the clusters post desodiation remained similar to that during sodiation in terms of length and width, probably owing to a non-monotonic relation during ion insertion.[21] The same was evident in the ortho slices of the *XZ*–axis after sodiation and desodiation, as shown in Figure 4d,f. Thus, the Sn clusters agglomerated in the pores, probably due to a lower surface energy. Moreover, the clusters stabilized at certain volumes, as shown in Figure S19h,i, Supporting Information.

To better understand the evolution of pore size inside CNF, the pore volume fractions of the central and edge subvolumes were calculated, as shown in Figure 4d,f. The central pore volume was relatively much lower than that of the edge in both the sodiated and desodiated states (Figure 4e,g). Notably, the dead volume of the pores inside the CNF was relatively low (below 1%, Figure S10, Supporting Information) despite the decrease in the volume of the central pore after sodiation (Figure 4e). The aforementioned results strongly confirmed that the pores in the CNF remained interconnected, which was beneficial for the good contact of Sn with the electrolyte, even at the central CNF region. Furthermore, the shapes of the pores were investigated by calculating their aspect ratio (Figure S20, Supporting Information). For pristine Sn–CNF, ≈40% of the pores had an aspect ratio ranging from 0.95 to 1.00, which represented the approximate spherical shape. The aspect ratio of the remaining 60% pores ranged from 0.25 to 0.80, representing a worm-like shape in combination with the tomography result of pores, shown in Figure 4d,f. For sodiated and desodiated Sn–CNF, the frequency of the approximate spherical-shaped pore reduced by 10%, while for the worm-like shaped pores, the frequency increased by 10%, possibly due to volume expansion from Sn cluster that led to the shape change (Figure S23, Supporting Information).

Despite changes in the pore size and pore volume upon sodiation and desodiation, the low dead volume fraction and highly interconnected nature of the pores suggested suppressed electrolyte decomposition at pores smaller than 2 nm, while the SEI layer was limited outside the pores in the CNF, as evidenced by the TEM images (Figure S24, Supporting Information). Moreover, the depth-profile X-ray photoelectron spectroscopy (XPS) (Figure S25 and Note S4, Supporting Information) revealed the ultra-thin nature of the SEI layer.

Based on the aforementioned analysis, Sn–CNF with interconnected pores (below 2 nm) was crucial for both high utilization of Sn sites and high ICE. Smaller pores (<2 nm) prevented SEI layer formation within the pores, and a high ICE was obtained. Moreover, the smaller pores remained interconnected, facilitating Na-ion transport within the CNF pores, particularly at the center, to ensure high utilization of Sn active sites.

3. Conclusion

We successfully synthesized CNF films with nanometer-sized interconnected pores to host Sn clusters (≈2 nm) and achieved high utilization (95%) of Sn active sites at a high rate of 1 A g^{-1}, while maintaining an improved ICE (87%). We applied STEM 3D reconstruction to reveal the "hidden" correlation between the pores and Sn clusters, and unambiguously unveiled the gradient and interconnected pores with Sn clusters at the carbon edge. The pore evolution during sodiation and desodiation identified the critical effect of pores on battery performance. With Na insertion, the pores in the CNF were flexible and remained interconnected, which was beneficial for fast kinetics and endowed high utilization of the Sn active sites at high currents. The nanometer-sized pores restricted electrolyte decomposition, and the SEI layer was limited to growth outside the CNF, thereby facilitating a high ICE The structural design of the pores in the CNF films combined the merits of high kinetics from nanosized particles and high stability from micronized CNF, thereby boosting the practical application of batteries and the precise solute sieving membrane design.

© 2024 Wiley-VCH GmbH

15214095, 0, Downloaded from https://onlinelibrary.wiley.com/doi/10.1002/adma.202307151 by li bai - Columbia University Libraries , Wiley Online Library on [27/02/2024]. See the Terms and Conditions (https://onlinelibrary.wiley.com/terms-and-conditions) on Wiley Online Library for rules of use; OA articles are governed by the applicable Creative Commons License

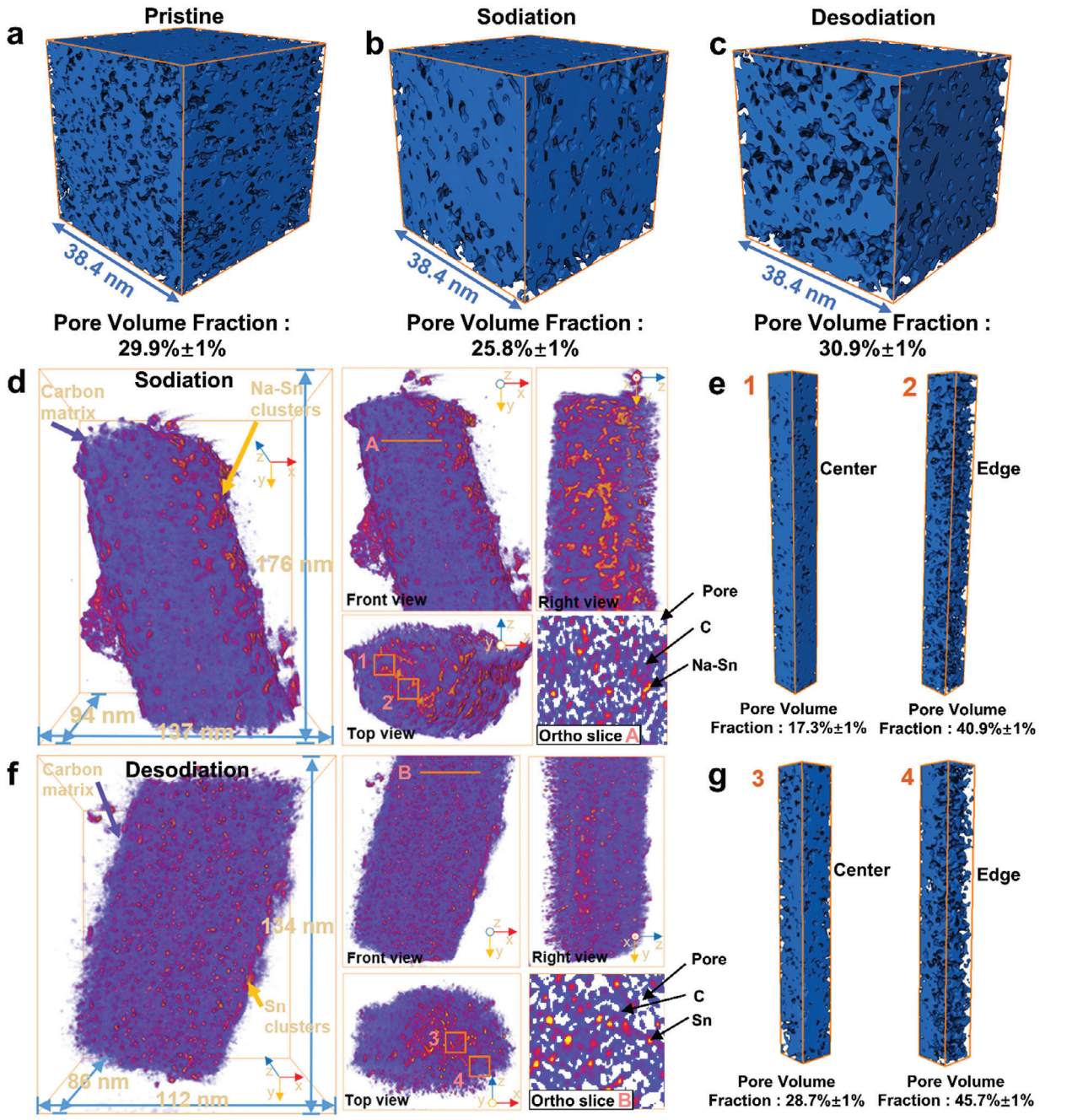

Figure 4. a–c) Schematic of pore volume fraction for pristine, sodiated, and desodiated Sn–CNF. d) 3D tomography of sodiated Sn–CNF and 38.4 × 38.4 nm ortho slice of *XZ*–axis from position A in (d), front view. e) Subvolume from (d), top view positions 1 and 2, and pore volume fraction of the sodiated Sn–CNF at the central and edge regions. f) 3D tomography of desodiated Sn–CNF and 38.4 × 38.4 nm ortho slice of *XZ*–axis from position B in (f), front view. g) Subvolume from (f), top view positions 3 and 4, and pore volume fraction of the desodiated Sn–CNF at the central and edge region.

4. Experimental Section

Preparation of Precursor Solution: PAN (0.5 g, $Mw = 150\,000$) and PVP (0.5 g, $Mw = 1\,300\,000$) were dried in an oven at 70 °C overnight, and then dissolved in 10 mL *N,N*-dimethylformamide at 60 °C with vigorous stirring overnight. $SnCl_2$ (0.8 g, anhydrous) was added to the solution and stirred overnight.

Preparation of Sn–CNF: The precursor solution was added to a 10 mL syringe and prepared through a 21 g stainless steel nozzle by applying a voltage of 15 kV, 15 cm from the collector, and covered with Cu foil. The flow rate of the syringe pump was set to 0.03 mm min^{-1}, while the electrospinning temperature was set to 50 °C. After 24 h of electrospinning, a white organic fiber mat was formed, which was dried at 60 °C for 10 h in an oven. Thereafter, the dried fiber mat was stabilized in a Muffle furnace at

© 2024 Wiley-VCH GmbH

15214095, 0, Downloaded from https://onlinelibrary.wiley.com/doi/10.1002/adma.202307151 by li bai - Columbia University Libraries , Wiley Online Library on [27/02/2024]. See the Terms and Conditions (https://onlinelibrary.wiley.com/terms-and-conditions) on Wiley Online Library for rules of use; OA articles are governed by the applicable Creative Commons License

280 °C for 5 h with a heating rate of 5 °C min^{-1}, then carbonized in H_2/Ar inside a tube furnace at 700 °C for 1 h and heating rate of 2 °C min^{-1}.

TEM Characterizations and 3D Reconstruction: TEM/STEM images, EELS/EDS spectra, and electron tomography experiments were performed using a CEOS probe-corrected FEI Themis TEM instrument (electron accelerating voltage of 300 kV) equipped with a Gatan image filter spectrometer. The probe convergence angle was 17.8 mrad, and the probe current was ≈50 pA for STEM imaging and EELS/EDS acquisition. EELS was performed with a Gatan Quantum 965 GIF system. Dual EELS was performed for simultaneous visualization of zero loss and M edges for calibration. The energy resolution was ≈0.9 eV, which was determined by the full-width at half-maximum of the zero-loss peak. Electron tomography experiments were performed on a Fischione tomography holder with a −80° to +80° tilt range. Seventy images were collected to perform reconstruction at a rate of 5.24 s per image. The reconstruction was performed using Thermo Fisher 3D Inspect and visualized in Avizo. The section "Data Processing of Tomography" discusses details on data processing. In situ TEM was performed using an in situ TEM-STEM sample holder (ZepTools Co., Ltd., China).

Other Characterizations: Microscopic structures were characterized by SEM (JEOL JSM-7100F). XRD patterns of the sample were collected via D8 Advance powder XRD with Cu Kα (λ = 1.5418 Å). The corresponding voltage and current parameters were 40 kV and 40 mA, respectively, and the test angle was 10–90°. The crystal structure evolution and phase transition mechanisms during charging and discharging were analyzed using in situ XRD. The XRD signals were acquired every 120 s in still mode. The cell for in situ XRD test was assembled with a removable battery mold, and the Sn–CNF film was placed on a Be window (owing to the oxidation of Be in air, peaks of BeO were observed in the result) to ensure passage of X-rays. The Raman spectra were acquired with an excitation laser (532 nm) using a Horiba LabRAM HR Evolution instrument. Thermogravimetric measurement (Netzsch STA 449C) was performed in atmosphere air from 30 to 700 °C at a heating rate of 5 °C min^{-1} to detect the content of Sn in Sn–CNF. XPS was performed using a VG Multilab 2000 system. BET test was conducted by ASAP 2020 Automatic Rapid Specific Surface Area and Porosity Analyzer (Micromeritics (Shanghai) Instrument Co. Ltd.). The XANES and EXAFS of the Sn K-edge were measured at beamline 7-BM (QAS) of the National Synchrotron Light Source II (NSLS-II), Brookhaven National Laboratory.

Data Processing of Tomography: All tomography data processing was performed using the Avizo software (Thermo Fisher 3D). The 3D tomography images (Figures 1e and 4d,f) were directly obtained using the "Volume Rendering" command and choosing a suitable rendering type and colormap. The rendering type was chosen as Standard, and the colormap was chosen as "temperature.icol" (the pore, Sn, and C were distinguished by different colors) with a suitable range. A reference box with "Bounding Box" command was included. The in/external volume fractions were then calculated as follows: The extracted subvolume commands were used for the internal and external parts, while the "Interactive Thresholding" command was applied to distinguish two different parts of Sn–CNF (pore, Sn&C&pore). With "Volume Rendering" command, the parts were shown as same-shaped cubes created by different parameter interactive thresholding, and the pore volume fraction was calculated as:

$$\text{Volume fraction} = \frac{V_{\text{Pore}}}{V_{\text{Sn\&C\&Pore}}} \times 100\% \quad (1)$$

The lengths and widths of the clusters and pores were determined using the maximum and minimum Feret diameters, respectively. The volume of the clusters and pores, which corresponded to the number of voxels of the object multiplied by the volume of a single voxel, was measured by

$$\text{Volume} = \text{Voxel count} \times cx \times cy \times cz \quad (2)$$

The dead-pore percentage was obtained using the "Fill Holes" and "Compute Ambient Occlusion" commands. All volume fractions were calculated in the same manner and each data point was reprocessed thrice to obtain the error bar.

Electrochemical Measurements: Electrochemical measurements were performed on CR2016 coin cells with Sn–CNF directly cut into electrode sheets as the working electrode, Na foil as the counter electrode, a glass microfiber filter (Whatman GF/D) as the separator, and 1 M $NaPF_6$ in DME as the electrolyte. All cells were assembled in an Ar-filled glovebox (MIKROUNA, Super) with O_2 and H_2O below 0.01 ppm. Constant current charge/discharge curves and cycling performance for half-cell were obtained on the Neware battery test system (BTS 4000) at room temperature within the potential ranging from 0.01–2.00 V (2.00–3.80 V for full-cell and pouch cell). CV and EIS results between 0.01 Hz and 100 kHz were obtained on the CORRTEST electrochemical workstation (CS3105). For a full-cell test, NVP was used as the cathode material, and the working electrode was prepared by mixing 70 wt% NVP, 20 wt% super P, and 10 wt% polytetrafluoroethylene, which was then rolled and cut into a suitable electrode sheet. The *N*/*P* ratio was set at 1:1.3. For pouch cells, the procedures were the same as those for the coin full-cell.

Supporting Information

Supporting Information is available from the Wiley Online Library or from the author.

Acknowledgements

H.M., R.Y., and Wa.X. contributed equally to this work. This work was supported by the Natural Science Foundation of China (22109123, 52201243), the Natural Science Foundation of Hubei Province (2022CFD090), the Sanya Science and Education Innovation Park of Wuhan University of Technology(2021KF0020), European Research Council (ERC) Starting Grant (805437-UltimateMembranes), and the Guangdong Basic and Applied Basic Research Foundation for financial support of the Research Grant (2021A1515111076). This study used beamline 7-BM (QAS) of the National Synchrotron Light Source II, a U.S. Department of Energy (DOE) Office of Science User Facility operated for the DOE Office of Science by Brookhaven National Laboratory under contract no. DE-SC0012704.

Conflict of Interest

The authors declare no conflict of interest.

Data Availability Statement

The data that support the findings of this study are available from the corresponding author upon reasonable request.

Keywords

3D reconstruction, high initial Coulombic efficiency, interconnected pores, Sn cluster

Received: July 19, 2023
Revised: January 1, 2024
Published online:

[1] a) J.-Y. Hwang, S.-T. Myung, Y.-K. Sun, *Chem. Soc. Rev.* **2017**, *46*, 3529; b) H. S. Hirsh, Y. Li, D. H. S. Tan, M. Zhang, E. Zhao, Y. S. Meng, *Adv. Energy Mater.* **2020**, *10*, 2001274; c) R. Usiskin, Y. Lu, J. Popovic, M. Law, P. Balaya, Y.-S. Hu, J. Maier, *Nat. Rev. Mater.* **2021**, *6*, 1020; d) M. Li, J. Lu, X. Ji, Y. Li, Y. Shao, Z. Chen, C. Zhong, K. Amine, *Nat. Rev. Mater.* **2020**, *5*, 276; e) H. Wang, F. Liu, R. Yu, J. Wu, *Interdiscip. Mater.* **2022**, *1*, 196.

© 2024 Wiley-VCH GmbH

15214095, 0, Downloaded from https://onlinelibrary.wiley.com/doi/10.1002/adma.202307151 by li bai - Columbia University Libraries , Wiley Online Library on [27/02/2024]. See the Terms and Conditions (https://onlinelibrary.wiley.com/terms-and-conditions) on Wiley Online Library for rules of use; OA articles are governed by the applicable Creative Commons License

[2] N. Tapia-Ruiz, A. R. Armstrong, H. Alptekin, M. A. Amores, H. Au, J. Barker, R. Boston, W. R. Brant, J. M. Brittain, Y. Chen, M. Chhowalla, Y.-S. Choi, S. I. R. Costa, M. Crespo Ribadeneyra, S. A. Cussen, E. J. Cussen, W. I. F. David, A. V. Desai, S. A. M. Dickson, E. I. Eweka, J. D. Forero-Saboya, C. P. Grey, J. M. Griffin, P. Gross, X. Hua, J. T. S. Irvine, P. Johansson, M. O. Jones, M. Karlsmo, E. Kendrick, et al., *JPhys Energy* **2021**, *3*, 031503.
[3] Z.-L. Xu, G. Yoon, K.-Y. Park, H. Park, O. Tamwattana, S. Joo Kim, W. M. Seong, K. Kang, *Nat. Commun.* **2019**, *10*, 2598.
[4] a) C. Zheng, D. Ji, Q. Yao, Z. Bai, Y. Zhu, C. Nie, D. Liu, N. Wang, J. Yang, S. Dou, *Angew. Chem., Int. Ed.* **2023**, *62*, e202214258; b) Y. Zhu, Q. Yao, R. Shao, C. Wang, W. Yan, J. Ma, D. Liu, J. Yang, Y. Qian, *Nano Lett.* **2022**, *22*, 7976.
[5] B. Zhu, G. Liu, G. Lv, Y. Mu, Y. Zhao, Y. Wang, X. Li, P. Yao, Y. Deng, Y. Cui, J. Zhu, *Sci. Adv.* **2019**, *5*, eaax0651.
[6] J. Y. Huang, L. Zhong, C. M. Wang, J. P. Sullivan, W. Xu, L. Q. Zhang, S. X. Mao, N. S. Hudak, X. H. Liu, A. Subramanian, H. Fan, L. Qi, A. Kushima, J. Li, *Science* **2010**, *330*, 1515.
[7] M. Chen, P. Xiao, K. Yang, B. Dong, D. Xu, C. Yan, X. Liu, J. Zai, C. J. Low, X. Qian, *Angew. Chem., Int. Ed.* **2023**, *62*, e202219177.
[8] a) M. Wagemaker, F. M. Mulder, *Acc. Chem. Res.* **2013**, *46*, 1206; b) P. Poizot, S. Laruelle, S. Grugeon, L. Dupont, J.-M. Tarascon, *Nature* **2000**, *407*, 496.
[9] R. Jain, A. S. Lakhnot, K. Bhimani, S. Sharma, V. Mahajani, R. A. Panchal, M. Kamble, F. Han, C. Wang, N. Koratkar, *Nat. Rev. Mater.* **2022**, *7*, 736.
[10] a) Q. Li, W. Zhang, J. Peng, W. Zhang, Z. Liang, J. Wu, J. Feng, H. Li, S. Huang, *ACS Nano* **2021**, *15*, 15104; b) Y. Wang, S. Luo, M. Chen, L. Wu, *Adv. Funct. Mater.* **2020**, *30*, 2000373.
[11] J. Liu, D. Xie, X. Xu, L. Jiang, R. Si, W. Shi, P. Cheng, *Nat. Commun.* **2021**, *12*, 3131.
[12] J. Scharf, M. Chouchane, D. P. Finegan, B. Lu, C. Redquest, M.-C. Kim, W. Yao, A. A. Franco, D. Gostovic, Z. Liu, M. Riccio, F. Zelenka, J.-M. Doux, Y. S. Meng, *Nat. Nanotechnol.* **2022**, *17*, 446.
[13] H. Kabbara, C. Noël, J. Ghanbaja, K. Hussein, D. Mariotti, V. Svrcek, T. Belmonte, *Sci. Rep.* **2015**, *5*, 17477.
[14] S. Müller, C. Sauter, R. Shunmugasundaram, N. Wenzler, V. De Andrade, F. De Carlo, E. Konukoglu, V. Wood, *Nat. Commun.* **2021**, *12*, 6205.
[15] Z. Lyu, D. Xu, L. Yang, R. Che, R. Feng, J. Zhao, Y. Li, Q. Wu, X. Wang, Z. Hu, *Nano Energy* **2015**, *12*, 657.
[16] B. Zhang, G. Rousse, D. Foix, R. Dugas, D. A. D. Corte, J.-M. Tarascon, *Adv. Mater.* **2016**, *28*, 9824.
[17] L. D. Ellis, T. D. Hatchard, M. N. Obrovac, *J. Electrochem. Soc.* **2012**, *159*, A1801.
[18] T. Palaniselvam, M. Goktas, B. Anothumakkool, Y. N. Sun, R. Schmuch, L. Zhao, B. H. Han, M. Winter, P. Adelhelm, *Adv. Funct. Mater.* **2019**, *29*, 1900790.
[19] a) R. Yu, Y. Pan, Y. Liu, L. Zhou, D. Zhao, J. Wu, L. Mai, *ACS Nano* **2023**, *17*, 2568; b) L. Zhang, Y. Liu, Y. You, A. Vinu, L. Mai, *Interdiscip. Mater.* **2023**, *2*, 91.
[20] C. J. Pelliccione, E. V. Timofeeva, C. U. Segre, *J. Phys. Chem. C* **2016**, *120*, 5331.
[21] a) S. Bi, H. Banda, M. Chen, L. Niu, M. Chen, T. Wu, J. Wang, R. Wang, J. Feng, T. Chen, M. Dinca, A. A. Kornyshev, G. Feng, *Nat. Mater.* **2020**, *19*, 552; b) T. Mo, S. Bi, Y. Zhang, V. Presser, X. Wang, Y. Gogotsi, G. Feng, *ACS Nano* **2020**, *14*, 2395.

© 2024 Wiley-VCH GmbH

15214095, 0, Downloaded from https://onlinelibrary.wiley.com/doi/10.1002/adma.202307151 by li bai - Columbia University Libraries , Wiley Online Library on [27/02/2024]. See the Terms and Conditions (https://onlinelibrary.wiley.com/terms-and-conditions) on Wiley Online Library for rules of use; OA articles are governed by the applicable Creative Commons License